Chinese Physics Letters

Spin transport properties in $MnBi_2Te_4$-based magnetic tunnel junctions

To cite this article before publication: Xinlong Dong *et al* 2023 *Chinese Phys. Lett.* in press https://doi.org/10.1088/0256-307X/40/8/087301

Spin transport properties in $MnBi_2Te_4$-based magnetic tunnel junctions

Xinlong Dong(董新龙)[1,2,3], Xin Jia(贾鑫)[1,2], Zhi Yan(严志)[2], Xuemin Shen(申学敏)[1,2], Zeyu Li(李泽宇)[3], Zhenhua Qiao(乔振华)*[3,4] and Xiaohong Xu(许小红)*[2]

1 College of Physics and Information Engineering, Shanxi Normal University, Taiyuan, Shanxi 030031, China

2 Key Laboratory of Magnetic Molecules and Magnetic Information Materials of the Ministry of Education, Research Institute of Materials Science, Shanxi Normal University, Taiyuan, Shanxi 030031, China

3 International Center for Quantum Design of Functional Materials, University of Science and Technology of China, Hefei, Anhui 230026, China

4 Hefei National Laboratory, University of Science and Technology of China, Hefei 230088, China

Corresponding author: qiao@ustc.edu.cn

Corresponding author: xuxh@sxnu.edu.cn

Abstract

The van der Waals heterojunctions, stacking of different two-dimensional materials, have opened unprecedented opportunities to explore new physics and device concepts. Here, combining density functional theory with non-equilibrium Green's function technique, we systematically investigate the spin-polarized transport properties of van der Waals magnetic tunnel junctions, Cu/$MnBi_2Te_4$ /$MnBi_2Te_4$/Cu and Cu/$MnBi_2Te_4$/*h*-BN/n-$MnBi_2Te_4$/Cu (n = 1, 2, 3). We find that the maximum TMR of Cu/$MnBi_2Te_4$/*h*-BN/3-$MnBi_2Te_4$/Cu MTJ can reach 162.6%, exceeding the system with only a single layer $MnBi_2Te_4$. More interestingly, our results indicate that Cu/$MnBi_2Te_4$/*h*-BN/n-$MnBi_2Te_4$/Cu (n = 2, 3) MTJs can realize the switching function, while Cu/$MnBi_2Te_4$/*h*-BN/3-$MnBi_2Te_4$/Cu MTJ exhibits the negative differential resistance. The Cu/$MnBi_2Te_4$/*h*-BN/3-$MnBi_2Te_4$/Cu in the parallel state shows a spin injection efficiency of more than 83.3%. Our theoretical findings of the transport properties will shed light on the possible experimental studies of $MnBi_2Te_4$-based van der Waals magnetic tunneling junctions.

Keywords: Magnetic tunnel junction, $MnBi_2Te_4$, tunneling magnetoresistance, van der Waals heterostructure

PACS: 73.23.-b; 85.75.-d

1. Introduction

The giant magnetoresistance (GMR) and tunnel magnetoresistance (TMR) effects play important roles in the fields of information storage technology and designing of spintronic devices [1-2]. Subsequently, the emergence of magnetic tunnel junctions (MTJs) prominently promoted the revolution of various spintronics [3-9]. Compared with traditional electronic devices, the magnetic recording density of MTJs-based devices can be considerably enhanced, leading to the miniaturization of electronic devices. So far, although much progress has been made, many problems and challenges still exist and need to be resolved for the improvement of the efficiency, performance, and stability of MTJs. For example, one of the research focuses is how to control the quality of the interface between the ferromagnetic layer and the barrier layer, because the interface influence's the transmission of electrons with different orbital properties and unequal spin polarization. Therefore, the interface bonding has a profound effect on the conductance. Fortunately, the layered two-dimensional materials supported by van der Waals (vdW) force without chemical bonding overcome these difficulties due to their advantages of layer-related thickness and ideal interface. Furthermore, constructing MTJs with two-dimensional materials also brings opportunities for exploring new physical phenomena and potential applications [10-17].

Since 2017, there has been great progress towards the development of two-dimensional (2D) magnetic materials. Numerous 2D materials have been synthesized experimentally [13-17], such as 2D ferromagnetic insulator CrI_3 and ferromagnetic metal Fe_3GeTe_2, providing abundant candidate materials to build MTJs. These 2D materials have been shown to be reliable platforms to construct high-performance MTJs through the layer-by-layer control of the thickness, sharp interfaces, and high perpendicular magnetic anisotropy. Compared with transition metal MTJs consisting of ferromagnetic electrodes and oxide barrier layers, it was reported that the van der Waals MTJs by 2D magnetic layers exhibit superior performance [18-31]. For instance, it was theoretically found that single/double-layer Fe_3GeTe_2-*h*BN-Fe_3GeTe_2 MTJs possessing prominent TMR effects, with the magnetoresistance ratio reaching up to 183% and 252%, respectively. And when the

Fe_3GeTe_2 MTJ is in the parallel state, a considerable spin polarization about 75% can be observed [21].

Later, layered $MnBi_2Te_4$ was successfully synthesized, and powder and single-crystal neutron diffraction measurements confirmed the intra-and inter-layer magnetic orders are ferromagnetic and antiferromagnetic, respectively [33, 34]. As an intrinsic magnetic topological insulator, several exotic topological states have been proposed, e.g., quantized topological magnetoelectric effect and quantum anomalous Hall effect [32–35]. Furthermore, our previous study [30] and Zhan et al.'s work [31] on $MnBi_2Te_4$-based MTJs reported that giant TMRs as well as high spin polarization could be induced. However, in these works, the effect of antiferromagnetic pinning layer on its transport properties was ignored. Therefore, it is necessary to explore the influence of the pinning layer on the $MnBi_2Te_4$-based MTJs.

In this work, we systematically study the spin current, spin injection efficiency (SIE), tunnelling magnetoresistance (TMR) and transmission coefficients of the Cu/$MnBi_2Te_4$/$MnBi_2Te_4$/Cu and Cu/$MnBi_2Te_4$/*h*-BN/n-$MnBi_2Te_4$/Cu (n = 1, 2, 3) MTJs by employing the non-equilibrium Green's function combined with density-functional theory. In the presence of pinning layer, we find that the maximum TMR of Cu/$MnBi_2Te_4$/*h*-BN/3-$MnBi_2Te_4$/Cu MTJ can reach 162.6%, exceeding the system with only a single layer $MnBi_2Te_4$. More interestingly, our results indicate that Cu/$MnBi_2Te_4$/*h*-BN/n-$MnBi_2Te_4$/Cu (n = 2, 3) MTJs can realize the switching function, while Cu/$MnBi_2Te_4$/*h*-BN/3-$MnBi_2Te_4$/Cu MTJ exhibits the negative differential resistance. Our findings demonstrate that the spin-related transport properties of these $MnBi_2Te_4$-based MTJs are highly dependent on the layer number and provide a promising platform for further experimental exploration of MTJs.

2. Model system and theoretical method

It is known that bilayer $MnBi_2Te_4$ is an insulator with A-type antiferromagnetic order [32]. Figure S1 shows the top and side views of the bilayer $MnBi_2Te_4$, respectively. Figure 1 (a-d) displays our considered system structure of

$MnBi_2Te_4$/*h*-BN/n-$MnBi_2Te_4$, where we utilize *h*-BN as the barrier layer and $MnBi_2Te_4$ as the ferromagnetic layer, respectively. The system is separated into three adjacent regions: the central scattering region, the left and the right electrodes (i.e., Cu (111)), respectively. When constructing the central region, we consider four cases (ignoring the buffer layers), i.e., Cu/$MnBi_2Te_4$/$MnBi_2Te_4$/Cu, Cu/$MnBi_2Te_4$/*h*-BN/$MnBi_2Te_4$/Cu, Cu/$MnBi_2Te_4$/*h*-BN/2-$MnBi_2Te_4$/Cu and Cu/$MnBi_2Te_4$/*h*-BN/3-$MnBi_2Te_4$/Cu MTJs.

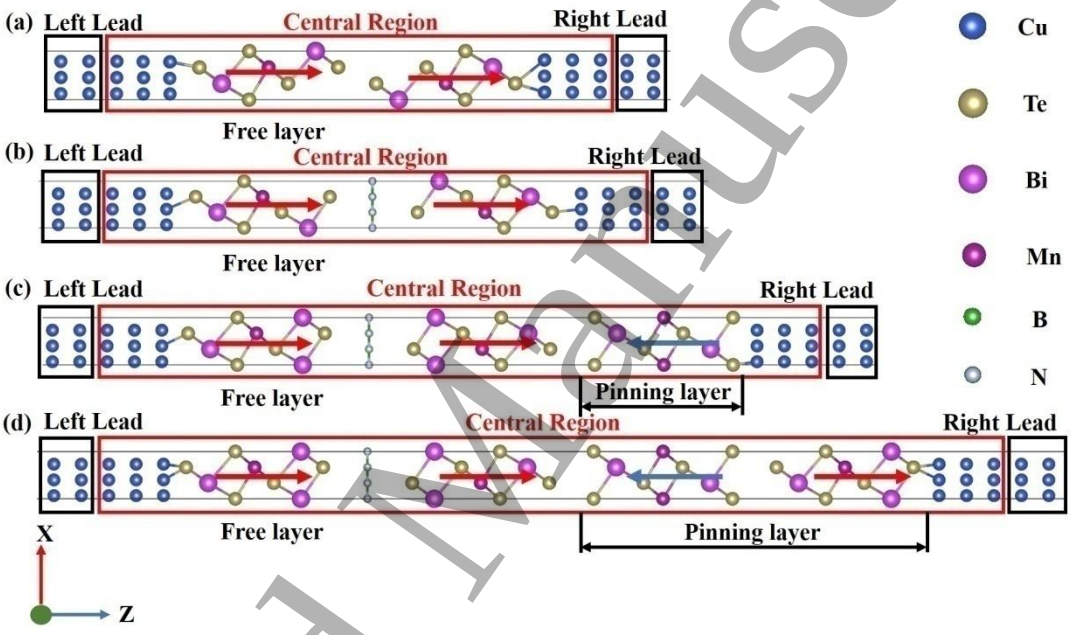

Fig. 1 Schematic diagrams of Cu/$MnBi_2Te_4$/$MnBi_2Te_4$/Cu, and Cu/$MnBi_2Te_4$/*h*-BN/n-$MnBi_2Te_4$/Cu (n = 1, 2, 3). The red and blue arrows represent the magnetic orientation of Mn atoms in the parallel (P) state. The antiparallel (AP) magnetization structure can be obtained by reversing the magnetic direction of the free layer . These devices are periodic in the X and Y directions, and the current flows in the Z direction.

Based on the nonequilibrium Green's function combined with density-functional theory, the spin-polarized current can be defined by the Landauer-Büttiker formula:

$$I_\sigma = \frac{e}{h}\int T_\sigma(E)\,[f_L(E) - f_R(E)]dE \qquad (1)$$

where$\sigma = \uparrow, \downarrow$denotes the index of spin, e is the electron charge, h is the Planck's constant, T_σ (E) is the spin-resolved transmission coefficient, and $f_{L(R)}$(E) is the Fermi-Dirac distribution function of the left (right) electrode.

The TMR ratio with different bias voltages can be expressed as [36, 37]:

$$TMR = \frac{R_{AP} - R_P}{R_P} = \frac{I_P - I_{AP}}{I_{AP}} \qquad (2)$$

where R_P and R_{AP} are the resistance across the stacked configuration when the magnetization of the ferromagnetic layer are parallel and antiparallel to each other, I_P and I_{AP} are the total currents across the devices when the magnetization of the ferromagnetic layer is in parallel (P) and antiparallel (AP) states. The spin injection efficiency (SIE) can be calculated by using $SIE = \frac{|I_\uparrow - I_\downarrow|}{|I_\uparrow + I_\downarrow|}$ [38]. In the equilibrium state, the TMR and SIE are estimated by using the transmission coefficient at the Fermi level.

All structural relaxation calculations were performed within the framework of density-functional theory as implemented in the Vienna ab initio simulation package (VASP) [39, 40]. The electron-core interaction was described by the projected augmented wave pseudopotential [41, 42] with the general gradient approximation (GGA) parameterized by Perdew, Burke, and Ernzerhof [43]. The electron wave function was expanded in plane waves up to a cutoff energy of 500 eV, and a 9×9×1 Monkhorst–Pack *k*-grid [44] was used to sample the Brillouin zone of the supercell. The convergence criterion for the electronic energy was set to be 10^{-5} eV. A vacuum region of 30 Å was used in the structural relaxation calculations of the central regions to avoid interaction between adjacent slabs. Moreover, van der Waals force was included by adopting the DFT-D2 method in all structural optimizations.

All electronic transport-related calculations are performed by using Nanodcal package based on non-equilibrium Green's function coupled with density functional theory (NEGF-DFT) [45, 46]. A linear combination based on atomic orbital (LCAO) basis sets composed of double-zeta polarized (DZP) functions was adopted. For self-consistent calculation, the convergence criterion of the Hamiltonian matrix is set to be 10^{-4} eV.

3. Results and discussion

In order to screen the influence of electrodes on the central scattering region, a long buffer layer is required to connect the left and the right electrodes to the central scattering region. By calculating the real spatial potential distribution of the system

center, whether the length of the buffer layer is sufficient. The results show that the potentials on the left and the right sides are smooth at the zone close to the electrode, indicating that the buffer layer can screen the influence of electrodes. In addition, there is a very high peak in the potential energy diagram corresponding to the position of *h*-BN, indicating that the insulating layer *h*-BN forms a barrier layer between $MnBi_2Te_4$ [as shown in Figure S2].

As shown in Figure 1, in the monolayer $MnBi_2Te_4$ adjacent to *h*-BN, if the magnetic moments of Mn atoms are along the same direction, the system is in the parallel (P) state. If the magnetic moments of Mn atoms are along the opposite directions, the system is in the antiparallel (AP) state. Meanwhile, the natural A-type antiferromagnetic configuration is set at the side with multilayer $MnBi_2Te_4$ [47].

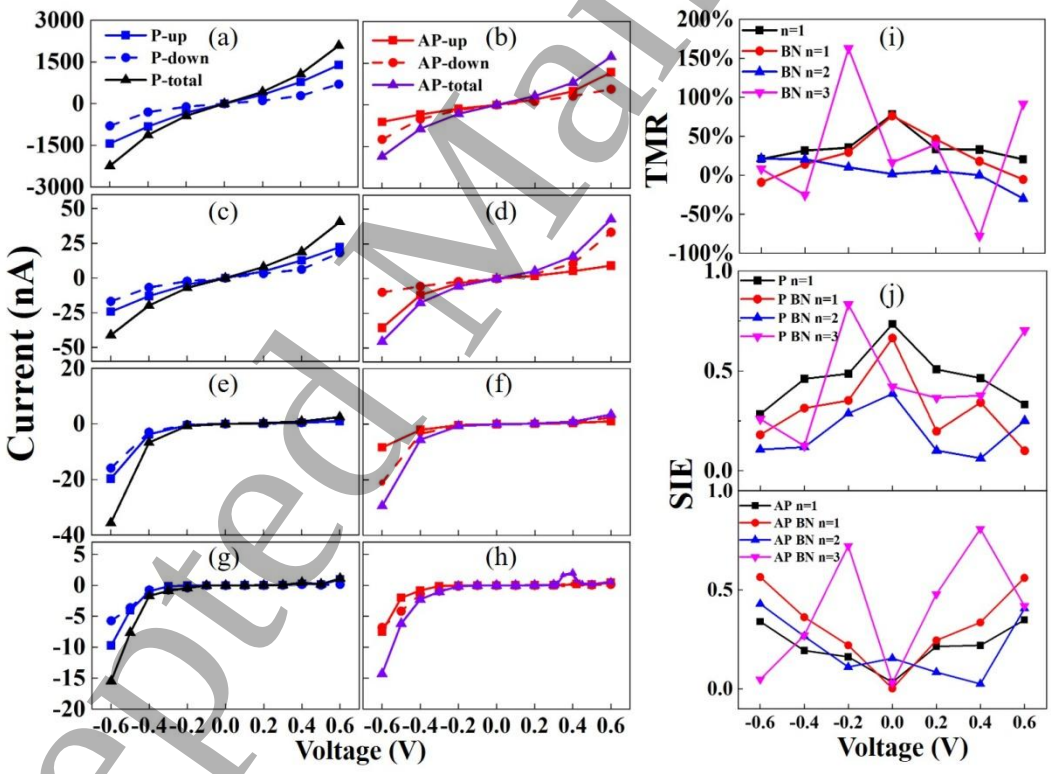

Fig. 2 (a)-(h) The I-V curves, TMR(i) and SIE(j) versus bias voltage of $Cu/MnBi_2Te_4/MnBi_2Te_4/Cu$ and $Cu/MnBi_2Te_4$/*h*-BN/n-$MnBi_2Te_4/Cu$ (n = 1, 2 and 3); Figure 2 (a) and (b) are corresponding to $Cu/MnBi_2Te_4/MnBi_2Te_4/Cu$ in the P state and AP state. Figure 2 (c, e, g) and (d, f, h) are corresponding to $Cu/MnBi_2Te_4$/*h*-BN/n-$MnBi_2Te_4/Cu$ (n = 1, 2 and 3) in the P states and AP states.

Figure 2 (a-h) shows the calculated I-V curves as a function of bias voltage ranging from -0.6 V to 0.6 V in the parallel and the antiparallel states for all

$MnBi_2Te_4$-based MTJs. The results indicate that for any bias, the spin current always increases in both up and down channels in the Cu/$MnBi_2Te_4$/$MnBi_2Te_4$/Cu and Cu/$MnBi_2Te_4$/*h*-BN/$MnBi_2Te_4$/Cu MTJs, and that of the Cu/$MnBi_2Te_4$/$MnBi_2Te_4$/Cu MTJ obviously exceeds that of the Cu/$MnBi_2Te_4$/*h*-BN/$MnBi_2Te_4$/Cu MTJ. As an insulator, the potential barrier formed by *h*-BN is much higher than that of vacuum layer, resulting in a significant decrease of current. For both structures, with the increase of bias, the spin-polarized current can be induced. When the Cu/$MnBi_2Te_4$/$MnBi_2Te_4$/Cu MTJ is in parallel state, the current in the spin-up channel increases linearly and is always larger than that in the spin-down channel for any bias. After switching the system to the antiparallel state, under positive bias, the current in the spin-up channel becomes larger than that of the spin-down channel. However, for negative bias, the current of the spin-down channel exceeds that of the spin-up channel. For the Cu/$MnBi_2Te_4$/*h*-BN/$MnBi_2Te_4$/Cu MTJ, the tendency of the current is the same as Cu/$MnBi_2Te_4$/$MnBi_2Te_4$/Cu MTJ in the parallel state. After switching the system to the antiparallel state, under positive bias, the current in the spin-down channel becomes larger than that of the spin-up channel. However, for negative bias, the current of the spin-up channel exceeds that of the spin-down channel. These results indicate that the spin-down and spin-up currents exhibit different behaviors under different positive and negative biases.

As displayed in Figure 2 (e), in the parallel state, the spin-up and -down currents are negligible within the range from -0.2 V to 0.3 V, leading to vanishing total current in Cu/$MnBi_2Te_4$/*h*-BN/2-$MnBi_2Te_4$/Cu MTJ. When the bias exceeds 0.4 V or -0.2 V, the spin-polarized current gradually increases. In the antiparallel state, the spin-polarized current is also suppressed when the bias is within the range from -0.1 V to 0.3 V. By further increasing the bias, the spin-polarized current can be observed. Therefore, these results indicate that there is a prominent switching effect in both parallel and antiparallel states. For the Cu/$MnBi_2Te_4$/*h*-BN/3-$MnBi_2Te_4$/Cu MTJ, the switching effect also emerges at a low bias range of (-0.1 V, 0.3 V). For the antiparallel state, the current reaches its maximum at the positive bias of 0.4 V. With

further bias increasing, the current decreases gradually, corresponding to the feature of the negative differential resistance effect, which is one of the most intriguing properties for its potential applications [48]. In short, the negative differential resistance effect characters that the current in a functional device decreases with the increase of the bias voltage in certain specific bias regions. It can be used to produce electronic molecular switch devices. The negative differential resistance effect is also a key component of some common electronic components such as diodes and resonant tunneling diodes.

The TMR of our $MnBi_2Te_4$-based MTJs is displayed in Figure 2 (i). At the equilibrium state, the TMR ratios of Cu/$MnBi_2Te_4$/$MnBi_2Te_4$/Cu and Cu/$MnBi_2Te_4$/*h*-BN/$MnBi_2Te_4$/Cu can reach 77.9% and 76%, respectively. In contrast, they can only reach 1.6% and 16.3% in Cu/$MnBi_2Te_4$/*h*-BN/2 -$MnBi_2Te_4$/Cu and Cu/$MnBi_2Te_4$/*h*-BN/3 -$MnBi_2Te_4$/Cu. With the increase of bias voltage, the TMR ratio decreases gradually and tends to be vanishing in Cu/$MnBi_2Te_4$/$MnBi_2Te_4$/Cu. For Cu/$MnBi_2Te_4$/*h*-BN/2 -$MnBi_2Te_4$/Cu system, when the positive bias increases to 0.6 V, the total current of antiparallel state increases prominently and exceeds the total current of parallel state, giving rise to a negative TMR ratio up to -30.6%. After the negative bias is applied, the current of parallel and antiparallel states will increase gradually in the bias range of (-0.2, -0.6 V), and the total current at the parallel state is larger than that at the antiparallel state, resulting in an enhanced TMR effect. For the Cu/$MnBi_2Te_4$/*h*-BN/3 -$MnBi_2Te_4$/Cu MTJ, when the bias voltage increases to 0.6 V, the current at the parallel state increases obviously, but the current at the antiparallel state decreases, resulting in a high TMR ratio about 91.1%. After the negative bias is applied, the current at the parallel state increases clearly at the bias voltage of -0.2 V, while the current at the antiparallel state is very limited. At the bias of -0.2 V, Cu/$MnBi_2Te_4$/*h*-BN/3 -$MnBi_2Te_4$/Cu possesses the maximum TMR ratio of 162.6%. It is well-known that MTJs with TMR ratios exceeding 100% can be used to produce both magnetic field sensors (key components of hard drives) and magnetoresistive random access memories. Therefore, Cu/$MnBi_2Te_4$/*h*-BN/3 -$MnBi_2Te_4$/Cu MTJ can be considered as a superior candidate to build spintronic devices.

Spin polarization is a key factor to determine the TMR performance, because a high spin-polarized current is essential to form a high magnetoresistance. Figure 2 (j) plots the spin injection efficiency of all $MnBi_2Te_4$-based MTJs at the parallel and antiparallel states, respectively. For the equilibrium state, the spin injection efficiency of the parallel state can reach 73.5% and 66.5% for Cu/$MnBi_2Te_4$/$MnBi_2Te_4$/Cu and Cu/$MnBi_2Te_4$/*h*-BN/$MnBi_2Te_4$/Cu MTJs, respectively. When Cu/$MnBi_2Te_4$/*h*-BN/3 -$MnBi_2Te_4$/Cu is at the antiparallel state, the spin injection efficiency can reach 80.9% under the bias voltage of 0.4 V. When Cu/$MnBi_2Te_4$/*h*-BN/3 -$MnBi_2Te_4$/Cu is at the parallel state, a higher spin injection efficiency can reach up to 83.3% at -0.2 V.

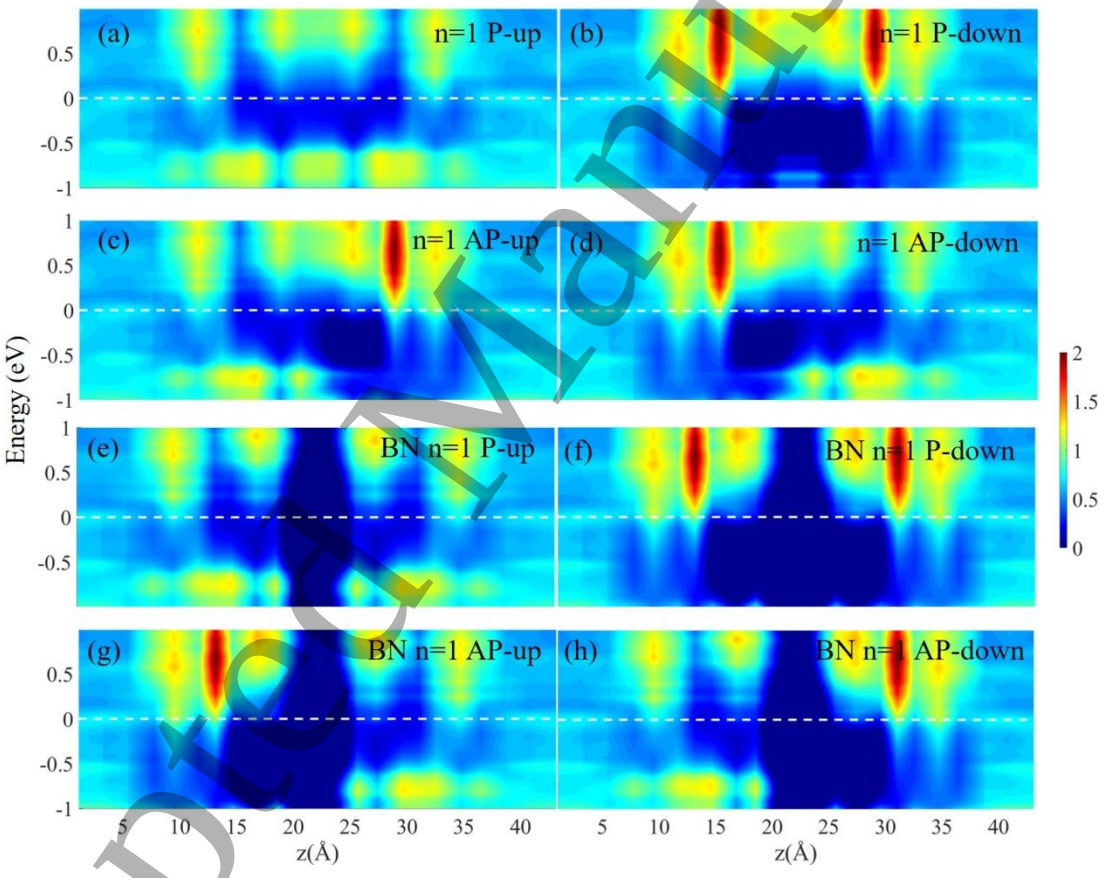

Fig. 3 The spin-resolved projected density of states (PDOS) along the transport direction (z-axis) of the parallel and antiparallel states of Cu/$MnBi_2Te_4$/$MnBi_2Te_4$/Cu and Cu/$MnBi_2Te_4$/*h*-BN/$MnBi_2Te_4$/Cu.

To visualize the spin-dependent transport properties, the real-space projected density of states along z direction are displayed in Figure 3. The spin-polarized transport channels in these $MnBi_2Te_4$-based MTJs are clearly seen. The dark blue zone around 23 Å is the barrier layer consisting of the vacuum layer and the *h*-BN in

the central region. Obviously, the vacuum layer and *h*-BN provide a barrier high enough to avoid the superposition of wave functions of $MnBi_2Te_4$ on both sides. Hereinbelow, we take Cu/$MnBi_2Te_4$/*h*-BN/$MnBi_2Te_4$/Cu MTJ as an example to demonstrate the physical mechanism. At the parallel state, for the spin-up electrons, there are two dark blue regions with few states near the Fermi level in Fig. 3(e), indicating a high resistance state. As displayed in Fig. 3(f), electrons in spin-down channel are majority states of $MnBi_2Te_4$ on both sides of *h*-BN at the Fermi level, which dominate the transport with a low resistance state. However, at the antiparallel state [see Figs. 3(g) and 3(h)], electrons in spin-up (spin-down) channels flow from the left $MnBi_2Te_4$, then penetrate *h*-BN with majority (minority) states, and then further flow into the right $MnBi_2Te_4$ with minority (majority) states. Thus, it generates a high resistance state for the Cu/$MnBi_2Te_4$/*h*-BN/$MnBi_2Te_4$/Cu MTJ. The above analysis can also be directly applied to Cu/$MnBi_2Te_4$/*h*-BN/2 -$MnBi_2Te_4$/Cu and Cu/$MnBi_2Te_4$/*h*-BN/3 -Mn Bi_2Te_4/Cu MTJs, as displayed in the Supplemental Material.

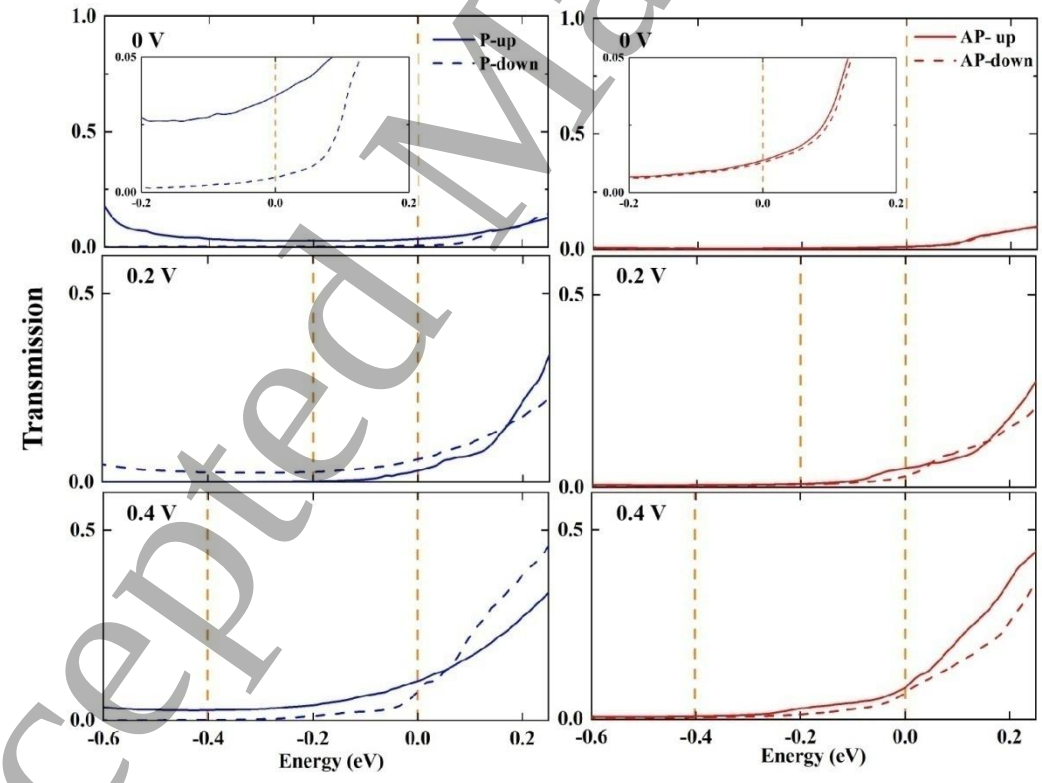

Fig. 4 Transmission coefficients as a function of energy at different bias voltages (0.0, 0.2 and 0.4 V) for Cu /$MnBi_2Te_4$/$MnBi_2Te_4$/Cu. Insets correspond to enlarged views of transmission coefficients near the Fermi level.

To further understand the TMR effect and the spin injection efficiency, we

investigate the non-equilibrium quantum transport properties by calculating the transmission coefficient at different bias voltages of these MTJs. According to Eq. (1), the current is finally determined by the transmission coefficient entering the integration interval. Figure 4 shows the transmission coefficients of $Cu/MnBi_2Te_4/MnBi_2Te_4/Cu$ MTJ as a function of energy at different bias voltages (0.0, 0.2, and 0.4 V). At the parallel state, one can find that there is an obvious spin polarization near the Fermi level, and the spin-up transmission coefficient is larger than that of spin-down. Therefore, the spin-up electrons contribute more to the transmission spectrum, leading to a significant spin injection efficiency at the equilibrium state. The corresponding spin injection efficiency and TMR ratio are 73.5% and 77.9%, respectively. See Supplemental Material for the transmission coefficients of $Cu/MnBi_2Te_4$/h-BN/$MnBi_2Te_4/Cu$, $Cu/MnBi_2Te_4$/h-BN/2-$MnBi_2Te_4/Cu$, and $Cu/MnBi_2Te_4$/*h*-BN/3-$MnBi_2Te_4/Cu$ MTJs. It is noteworthy that the bias tunability of spin polarization and TMR, together with the negative differential resistance, may pave the way for the development of high-performance spin-based magnetic detection and high-frequency logic devices.

4. Conclusions

The electronic transport properties of $Cu/MnBi_2T_4/MnBi_2Te_4/Cu$ and $Cu/MnBi_2Te_4$/*h*-BN/n-$MnBi_2Te_4/Cu$ (n = 1, 2, 3) MTJs are systematically studied by using nonequilibrium Green's function and density-functional theory. At both parallel and antiparallel states, $Cu/MnBi_2Te_4$/*h*-BN/n-$MnBi_2Te_4/Cu$ (n = 2, 3) MTJs exhibit huge potential as switching devices at the bias range of (0.0, 0.3 V). Particularly, the maximum TMR ratio of $Cu/MnBi_2Te_4$/*h*-BN/3-$MnBi_2Te_4/Cu$ can reach 162.6%. At the antiparallel state, there is a significant negative differential resistance effect in $Cu/MnBi_2Te_4$/*h*-BN/3-$MnBi_2Te_4/Cu$. Our results provide important theoretical guidance for further study of $MnBi_2T_4$-based van der Waals magnetic tunnel junctions.

ACKNOWLEDGMENTS

This work was financially supported by the Natural Science Basic Research Progrom of Shanxi (No. 20210302124252).

References

[1] Prinz G A 1998 *Science* **282** 1660

[2] Wolf S A, Awschalom D D, Buhrman R A, Daughton J M, von Molnár S, Roukes M L, Chtchelkanova A Y, and Treger D M 2001 *Science* **294** 1488

[3] Chappert C, Fert A, and Van Dau F N 2007 *Nat. Mater.* **6** 813

[4] Wood R 2009 *J. Magn. Magn. Mater.* **321** 555

[5] Khvalkovskiy A V, Apalkov D, Watts S, Chepulskii R, Beach R S, Ong A, Tang X, Driskill-Smith A, Butler W H, and Visscher P B 2013 *J. Phys. D: Appl. Phys.* **46** 074001

[6] Jia X T, and Xia K 2014 *Front. Phys.* **9** 768

[7] Zhuang J, Wang Y, Zhou Y, Wang J, and Guo H 2017 *Front. Phys.* **12** 127304

[8] Lan G, Xu H, Zhang Y, Cheng C, He B, Li J, He C, Wan C, Feng J, Wei H, Zhang J, Han X, and Yu G 2023 *Chin. Phys. Lett*. **40** 058501

[9] Zhu W, Xie S, Lin H, Zhang G, Wu H , Hu T, Wang Z, Zhang X, Xu J, Wang Y, Zheng Y, Yan F, Zhang J, Zhao L, Patan A, Zhang J, Chang H, and Wang K 2022 *Chin. Phys. Lett*. **39** 128501

[10] Burch K S, Mandrus D, and Park J G 2018 *Nature* **563** 47

[11] Gong C, and Zhang X 2019 *Science* **363** eaav4450

[12] Chen W, Sun Z, Wang Z, Gu L, Xu X, Wu S, and Gao C 2019 *Science* **366** 987

[13] Fei Z, Huang B, Malinowski P, Wang W, Song T, Sanchez J, Yao W, Xiao D, Zhu X, May A F, Wu W, Cobden D H, Chu J, and Xu X 2018 *Nat. Mater*. **17** 782

[14] Deng Y, Yu Y, Song Y, Zhang J, Wang N Z, Sun Z, Yi Y, Wu Y Z, Wu S, Zhu J, Wang J, Chen X H, and Zhang Y 2018 *Nature* **563** 94

[15] Gong C, Li L, Li Z, Ji H, Stern A, Xia Y, Cao T, Bao W, Wang C, Wang Y, Qiu Z, Cava R J, Louie S G, Xia J, and Zhang X 2017 *Nature* **546** 265

[16] Bonilla M, Kolekar S, Ma Y, Diaz H C, Kalappattil V, Das R, Eggers T,. Gutierrez H R, Phan M H, and Batzill M 2018 *Nat. Nanotechnol.* **13** 289

[17] Huang B, Clark G, Klein D R, MacNeill D, Navarro-Moratalla E, Seyler K L, Wilson N, McGuire M A, Cobden D H, Xiao D, Yao W, Jarillo-Herrero P, and Xu X 2018 *Nat. Nanotechnol.* **13** 544

[18] Li X, Lu J T, Zhang J, You L, Su Y, and Tsymbal E Y 2019 *Nano Lett.* **19** 5133

[19] Yan Z, Zhang R, Dong X, Qi S, and Xu X 2020 *Phys. Chem. Chem. Phys*. **22** 14773

[20] Pan L, Huang L, Zhong M, Jiang X W, Deng H X, Li J, Xia J B, and Wei Z 2018 *Nanoscale* **10** 22196

[21] Lin Z Z, and Chen X 2020 *Adv. Electron. Mater.* **6** 1900968

[22] Zhang L, Li T, Li J, Jiang Y, Yuan J, and Li H 2020 *J. Phys. Chem. C* **124** 27429

[23] Wang Z, Sapkota D, Taniguchi T, Watanabe K, Mandrus D, and Morpurgo A F 2018 *Nano Lett*. **18** 4303

[24] Zhou J, Qiao J, Duan C G, Bournel A, Wang K L, and Zhao W 2019 *ACS Appl. Mater. Interfaces* **11** 17647

[25] Pan L, Wen H, Huang L, Chen L, Deng H X, Xia J B, and Wei Z 2019 *Chin. Phys. B* **28** 107504

[26] Wu X, Feng Y, Li S, Zhang B, and Gao G 2020 *J. Phys. Chem. C* **124** 16127

[27] Feng Y, Liu N, and Gao G 2021 *Appl. Phys. Lett.* **118** 112407

[28] Feng Y, Wu X, Hu L, and Gao G 2020 *J. Mater. Chem. C* **8** 14353

[29] Feng Y, Wu X, and Gao G 2020 *Appl. Phys. Lett.* **116** 022402

[30] Yan Z, Jia X, Shi X, Dong X, and Xu X 2021 *Appl. Phys. Lett*. **118** 223503

[31] Zhan G, Yang Z, Luo K, Zhang D, Lou W, Liu J, Wu Z, and Chang K, 2022 *MRS Bull*. **47** 1177

[32] Zhang D, Shi M, Zhu T, Xing D, Zhang H, and Wang J 2019 *Phys. Rev. Lett.* **122** 206401

[33] Gong Y, Guo J, Li J, Zhu K, Liao M, Liu X, Zhang Q, Gu L, Tang L, Feng X, Zhang D, Li W, Song C, Wang L, Yu P, Chen X, Wang Y, Yao H, Duan W, Xu Y, Zhang S C, Ma X, Xue Q K, and He K 2019 *Chin. Phys. Lett.* **36** 076801

[34] Li J, Li Y, Du S, Wang Z, Gu B L, Zhang S C, He K, Duan W, and Xu Y 2019 *Sci. Adv*. **5** 2375

[35] Wang H, Wang D, Yang Z, Shi M, Ruan J, Xing D, Wang J, and Zhang H 2020 *Phys. Rev. B* **101** 081109

[36] Yuasa S, Nagahama T, Fukushima A, Suzuki Y, and Ando K 2004 *Nat. Mater.* **3** 868

[37] Parkin S S, Kaiser C, Panchula A, Rice P M, Hughes B, Samant M, and Yang S H 2004 *Nat. Mater.* **3** 862

[38] Zhang S, Xie Y, Hu Y, Niu X, and Wang Y 2018 *Phys. Chem. Chem. Phys.* **20** 29440

[39] Kresse G, and Hafner J 1993 *Phys. Rev. B* **48** 13115

[40] Kresse G, and Furthmuller J 1996 *Comput. Mater. Sci.* **6** 15

[41] Blöchl P E 1994 *Phys. Rev. B* **50** 17953

[42] Kresse G, and Joubert D 1999 *Phys. Rev. B* **59** 1758

[43] Perdew J P, Burke K, and Ernzerhof M 1996 *Phys. Rev. Lett.* **77** 3865

[44] Monkhorst H J, and Pack J D 1976 *Phys. Rev. B* **13** 5188

[45] Taylor J, Guo H, and Wang J 2001 *Phys. Rev. B* **63** 245407

[46] Taylor J, Guo H, and Wang J 2001 *Phys. Rev. B* **63** 121104

[47] Xing W, Qiu L, Wang X, Yao Y, Ma Y, Cai R, Jia S, Xie X C, and Han W 2019 *Phys. Rev. X* **9** 011026

[48] Kuang G, Chen S Z, Yan L, Chen K Q, Shang X, Liu P N, and Lin N 2018 *J. Am. Chem. Soc.* **140** 570

Support information

Spin transport properties in $MnBi_2Te_4$-based magnetic tunnel junctions

Xinlong Dong[1,2,3], Xin Jia[1,2], Zhi Yan[2], Xuemin Shen[1,2], Zeyu Li[3], Zhenhua Qiao*[3,4] and Xiaohong Xu*[2]

1 College of Physics and Information Engineering, Shanxi Normal University, Taiyuan, Shanxi 030031, China

2 Key Laboratory of Magnetic Molecules and Magnetic Information Materials of the Ministry of Education, Research Institute of Materials Science, Shanxi Normal University, Taiyuan, Shanxi 030031, China

3 International Center for Quantum Design of Functional Materials, University of Science and Technology of China, Hefei, Anhui 230026, China

4 Hefei National Laboratory, University of Science and Technology of China, Hefei 230088, China

Corresponding author: qiao@ustc.edu.cn

Corresponding author: xuxh@sxnu.edu.cn

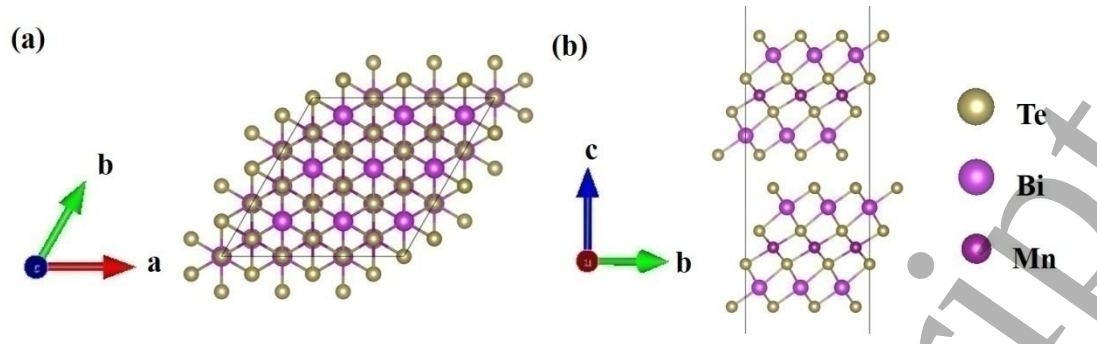

Fig. S1 The top (a) and side (b) view of the bilayer $MnBi_2Te_4$.

Figure S1 shows the top (a) and side views (b) of the bilayer $MnBi_2Te_4$, respectively. $MnBi_2Te_4$ is a layered ternary tetradymite compound with the space group of $R\bar{3}m$, which consists of Te-Bi-Te-Mn-Te-Bi-Te SL stacking through van der Waals (vdWs) force.

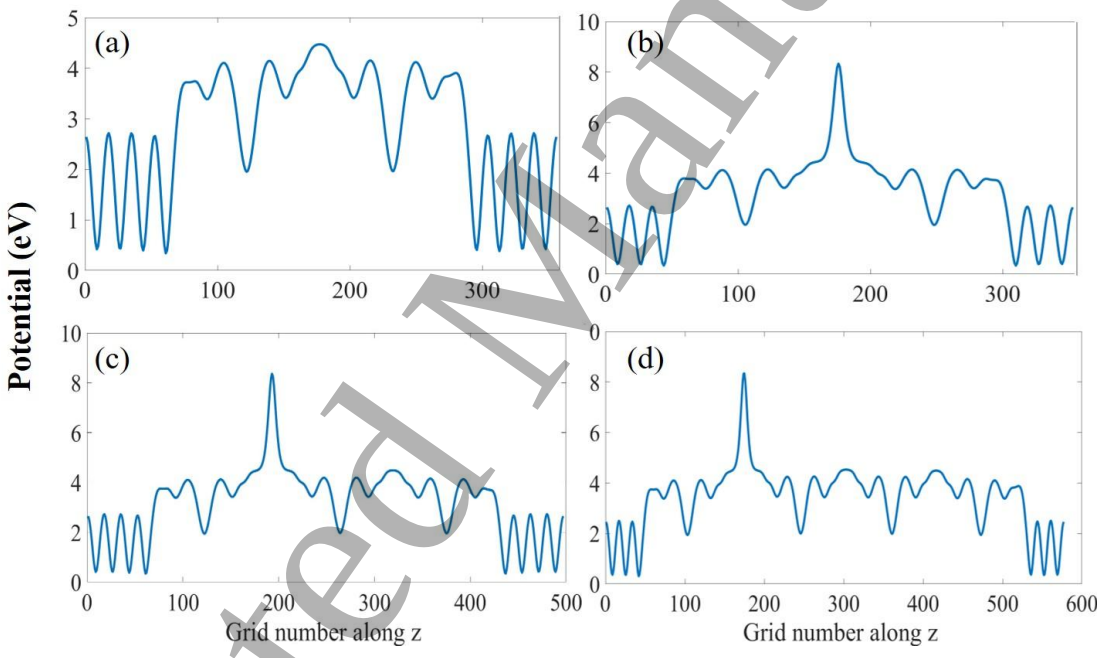

Fig. S2 The potential distribution of $Cu/MnBi_2Te_4/MnBi_2Te_4/Cu$, and $Cu/MnBi_2Te_4/h$-BN/n-$MnBi_2Te_4/Cu$ (n = 1, 2, 3), respectively. The wave lines on the left and right sides correspond to the buffer layer, and the peak value in the middle represents the barrier layer.

As shown in Figure S2, by calculating the real spatial potential distribution of the system center, we can determine whether the length of the buffer layer is sufficient. The results show that the potentials on the left and the right sides are smooth at the zone close to the electrode, indicating that the buffer layer can screen the influence of electrodes. It is demonstrated that three layers of Cu are enough to screen the scattering potential of the central region.

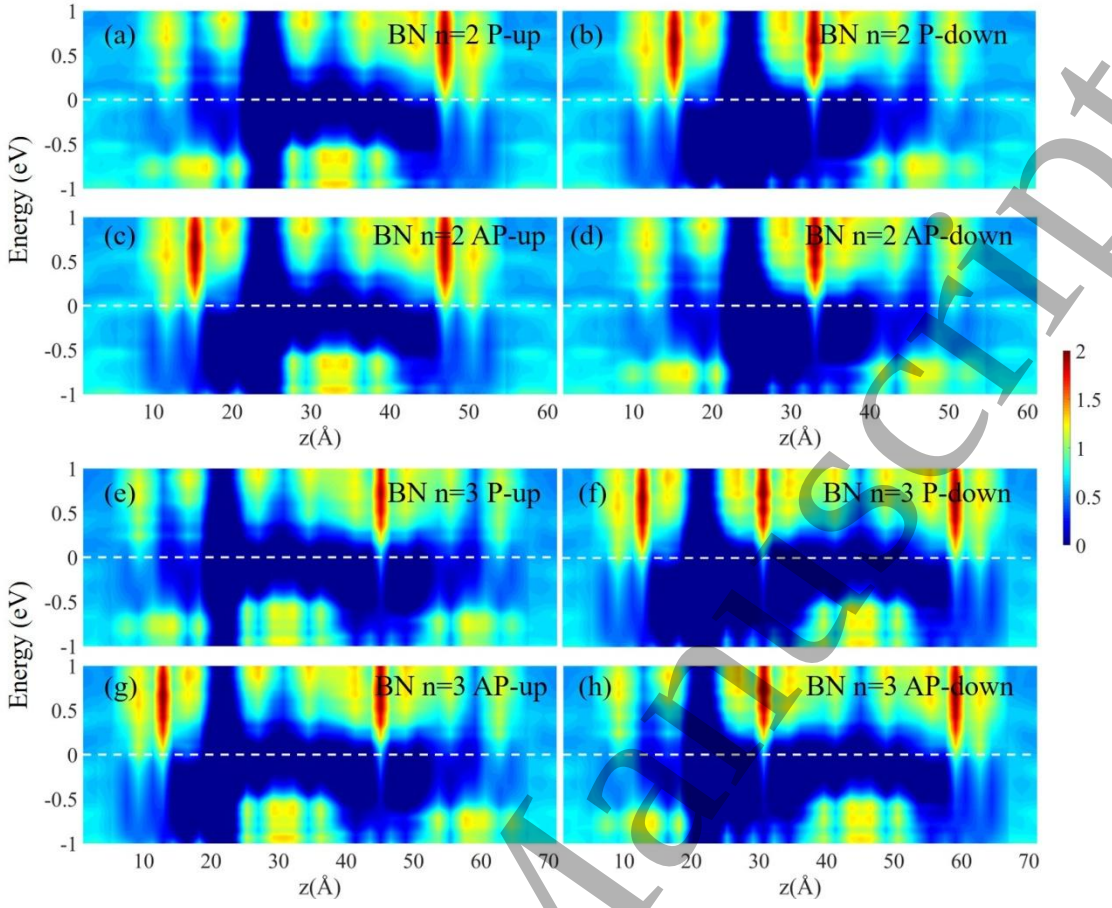

Fig. S3 The spin-resolved projected density of states (PDOS) of the parallel and antiparallel states of Cu/$MnBi_2Te_4$/*h*-BN/2-$MnBi_2Te_4$/Cu (a-d) and Cu/$MnBi_2Te_4$/*h*-BN/3-$MnBi_2Te_4$/Cu (e-h).

Figure S3 shows the spin-resolved projected density of states (PDOS) along the transport direction (z-axis) of the parallel and antiparallel states of Cu/$MnBi_2Te_4$/*h*-BN/2-$MnBi_2Te_4$/Cu and Cu/$MnBi_2Te_4$/*h*-BN/3-Mn Bi_2Te_4/Cu. At the parallel state, for the spin-up electrons, there are two dark blue regions with few states near the Fermi level in Fig. S3(a) and Fig. S3(e), indicating a high resistance state. As displayed in Fig. S3(b) and Fig. S3(f), electrons in spin-down channel are majority states of $MnBi_2Te_4$ on both sides of *h*-BN at the Fermi level, which dominate the transport with a low resistance state. However, at the antiparallel state, electrons in spin-up channels [see Figs. S3(c) and S3(g)] flow from the left $MnBi_2Te_4$, then penetrate *h*-BN with majority states, and then further flow into the right $MnBi_2Te_4$ with minority states, electrons in spin-down channels [see Figs. S3(d) and S3(h)] flow from the left $MnBi_2Te_4$, then penetrate *h*-BN with minority states, and then further flow into the right $MnBi_2Te_4$ with majority states. Thus, it generates a high resistance

state for the Cu/$MnBi_2Te_4$/*h*-BN/2 -$MnBi_2Te_4$/Cu and Cu/$MnBi_2Te_4$/*h*-BN/3 -Mn Bi_2Te_4/Cu.

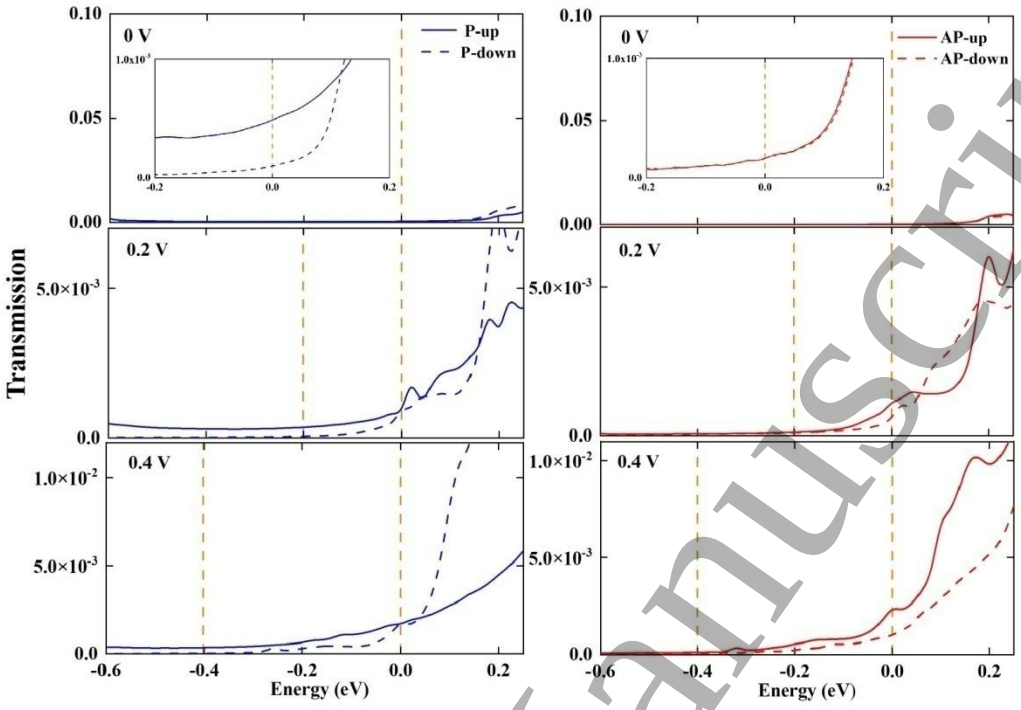

Fig. S4 Transmission coefficients as a function of energy at different bias voltages (0, 0.2 and 0.4 V) for Cu/$MnBi_2Te_4$/*h*-BN/$MnBi_2Te_4$/Cu. Insets correspond to enlarged views of transmission coefficients near the Fermi level.

Figure S4 displays the transmission coefficients as a function of energy at different bias voltages (0.0, 0.2, and 0.4 V) for parallel and antiparallel states of Cu/$MnBi_2Te_4$/*h*-BN/$MnBi_2Te_4$/Cu MTJ, respectively. In parallel state, there is visible spin polarization at the Fermi level leading to a higher spin injection efficiency. The spin injection efficiency decreased significantly at the bias of 0.2 V. The corresponding transmission coefficients show that the spin up and spin down electron transmission spectra almost overlap mutually, so the spin injection efficiency decreased significantly. In antiparallel state, there is almost no spin-polarization. Hence, it shows that the spin injection efficiency is only 0.2 %. Under the bias voltage of 0.2 V, the transmission coefficients of spin up and down increase, resulting in enhanced spin injection efficiency.

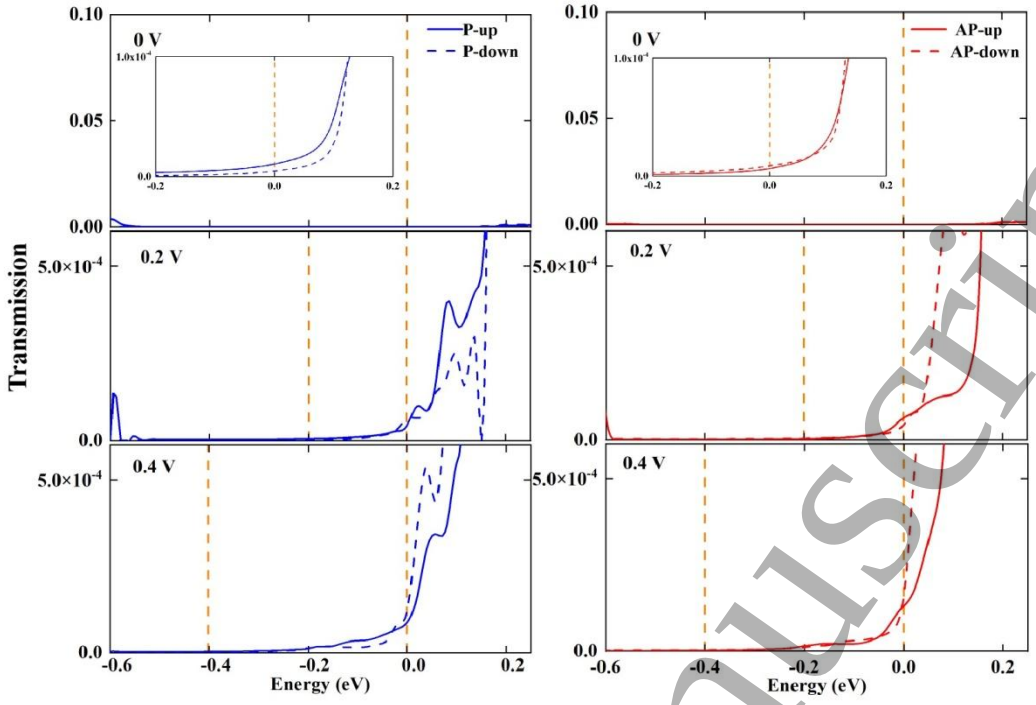

Fig. S5 Transmission coefficients as a function of energy at different bias voltages (0, 0.2 and 0.4 V) for Cu/$MnBi_2Te_4$/*h*-BN/2-$MnBi_2Te_4$/Cu. Insets correspond to enlarged views of transmission coefficients near the Fermi level.

Figure S5 displays the transmission coefficients as a function of energy at different bias voltages (0.0, 0.2, and 0.4 V) for parallel and antiparallel states of Cu/$MnBi_2Te_4$/*h*-BN/2-$MnBi_2Te_4$/Cu MTJ, respectively. In the equilibrium state, there is almost no net spin polarization in the antiparallel state, the corresponding spin injection efficiency is only 3%. Compared to the equilibrium state, the integral of transmission coefficient at 0.2 V has little change. When the bias is increased to 0.4 V, the integral of transmission coefficient is obviously larger than that of 0.2 V. These results explain the switching effect.

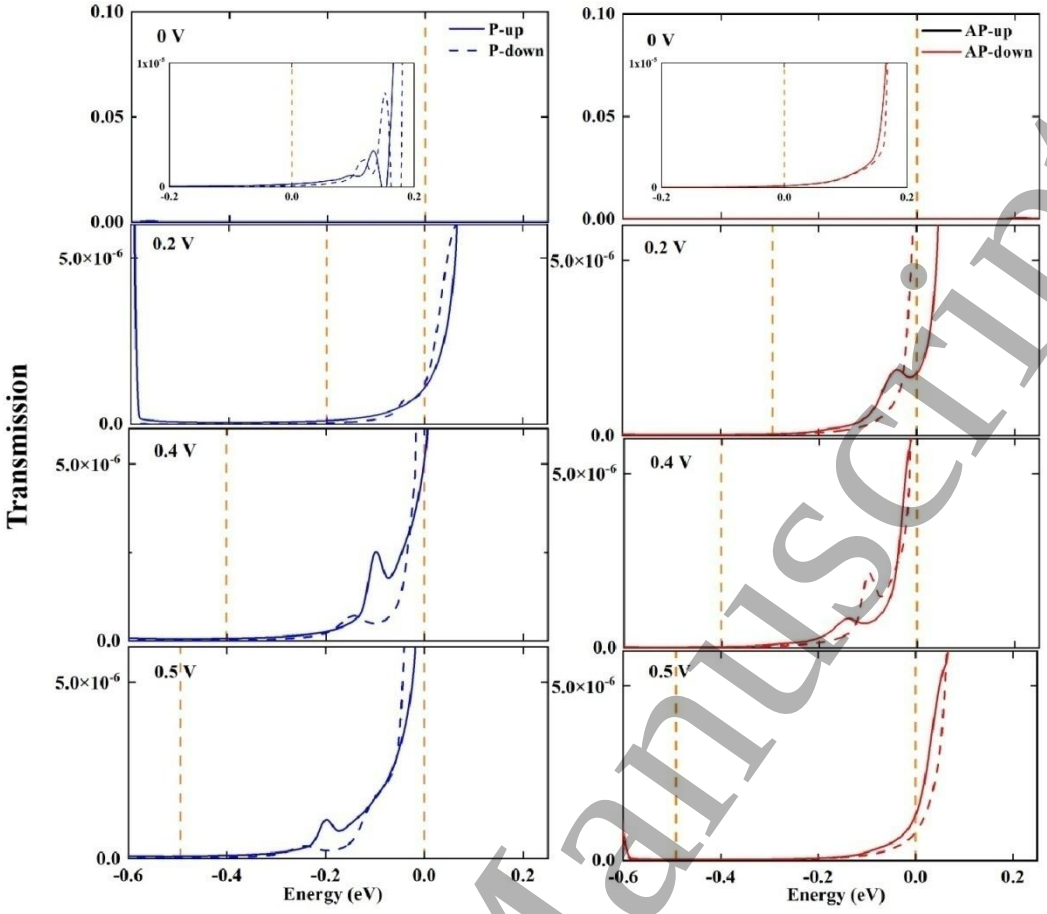

Fig. S6 Transmission coefficients as a function of energy at different bias voltages (0, 0.2, 0.4 and 0.5 V) for Cu/$MnBi_2Te_4$/*h*-BN/3 -$MnBi_2Te_4$/Cu. Insets correspond to enlarged views of transmission coefficients near the Fermi level.

Figure S6 displays the transmission coefficients as a function of energy at different bias voltages (0.0, 0.2, 0.4, and 0.5 V) of respective parallel and antiparallel states of Cu/$MnBi_2Te_4$/*h*-BN/3 -$MnBi_2Te_4$/Cu MTJ. At the equilibrium state, the spin polarization for either parallel or the antiparallel state is negligible, corresponding to the weak spin injection efficiency of only 42% and 3%, respectively. Furthermore, at the antiparallel state, the integral of spin-down transmission coefficient at 0.4 V is larger than those at 0.2 V and 0.5 V as shown in Fig. S6. This explains that the current first increases and then decreases with the increase of bias voltage from 0.2 V to 0.5 V, giving rise to negative differential resistance.